# Theoretical Study of sp²-sp³ Hybridized Carbon Network for Li-ion Battery Anode

Y. W. Wen,[†] Xiao Liu,[†] Xianbao Duan,[†] Kyeongjae Cho,[§] Rong Chen,*[‡] and Bin Shan*[†,§]

[†]State Key Laboratory of Material Processing and Die and Mold Technology and School of Materials Science and Engineering and
[‡]State Key Laboratory of Digital Manufacturing Equipment and Technology and School of Mechanical Science and Engineering, Huazhong University of Science and Technology, Wuhan 430074, Hubei, People's Republic of China
[§]Department of Materials Science and Engineering, The University of Texas at Dallas, Richardson, Texas 75080, United States

Ⓢ Supporting Information

**ABSTRACT:** We discover through first-principles calculations a new type of nanoporous carbon network structure formed out of small diameter nanotubes that features unique sp²-sp³ bonding hybridizations and highly ordered 1-D channels for Li-ion diffusion. Unlike other graphitic materials that are primarily bonded by intertube/interlayer van der Waals forces, the predicted sp²-sp³ hybridized carbon networks (HCNs) are held together by strong sp³ covalent bonding at the junctions, with sp²-hybridized interconnects providing conducting π-electrons near the Fermi level. With well-aligned and size-tunable 1-D nanopores, we show that besides desirable high Li capacity, stable Li-ion intercalation voltage profile, and low diffusion barriers, the volumetric change of HCN between fully lithiated/delithiated phases is <1%, making it a very promising Li-ion battery anode candidate.
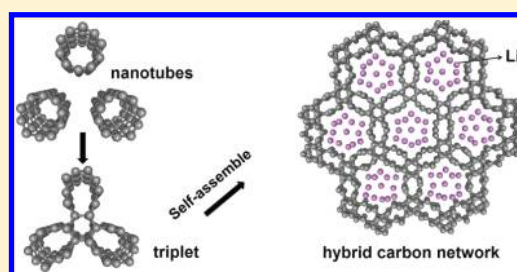
## 1. INTRODUCTION

Li-ion battery (LIB) is an attractive power source due to its high energy density and has found wide applications in portable electronics and electrical vehicles. As a key component of LIB, the anode material is desired to have a high Li capacity, low oxidation−reduction potentials, high-rate Li diffusivity, and a stable mechanical structure. Graphite, a low-cost carbon material developed by Sony laboratories in the 1990s, is still the most widely used material for commercial LIB anodes.[1] However, with a specific capacity of 372 mAh/g and tendency toward exfoliation upon extended charging cycles, it faces a number of challenges for use in longer-lasting, higher-capacity LIBs. Extensive research has been carried out to improve both the mechanical robustness and specific capacity of anodes.[2−14] Among various carbon materials investigated so far, carbon nanotube (CNT)-derived structures have attracted much attention for their high porosity, large surface area, and excellent electrical conductivity. It has been theoretically predicated that bundles of CNT could achieve much higher Li capacity than graphite, primarily due to Li storage in the interstitial sites between neighboring CNTs.[3,15] However, Li-ion intercalation into these van der Waals (vdW)-interaction-dominated intertube sites may cause considerable lattice expansion, and such expansion of bundles would eventually destroy the patterned CNT structures.[16,17] Moreover, because of the lack of strong interactions, as-fabricated CNTs easily become entangled and favor the formation of solid electrolyte interphase (SEI), which is the primary source of reversible capacity decay over extended cycling.[12,18] Graphene is another promising LIB anode material whose reversible capacity is substantial and can be further enhanced by means of doping or etching into nanoribbons.[6,19−22] Yoo et. al reported $C_{60}$-intercalated graphene nanosheets with enlarged interlayer spacing that could boost specific capacity to 784 mAh/g.[23] However, weak vdW interactions also cause 19% lattice expansion during Li intercalation and lead to similar problems in structural stability.

It can thus be deduced that mechanical robustness is crucial for graphitic LIB anodes in preventing exfoliation and fading of capacity upon cycling, yet it is hard to prevent structural fractures in graphitic systems, primarily because Li intercalation generally takes place in the interlayer or intertube spacing, where weak vdW forces dominate. We report a nanoporous hybridized carbon network (HCN) structure that completely eliminates weak vdW interactions and substitutes them with strong sp³-hybridized covalent bonds in the junction regions, providing extreme mechanical robustness, yet retaining good electronic conductivity at the Fermi level by maintaining the sp² hybridization in the interconnect regions. The sp²-sp³ hybridized network structure could increase mechanical robustness and effectively avoid the entangling issue in single-wall carbon nanotubes (SWNTs). Moreover, the surface area of HCN is much smaller than that of SWNTs due to covalent tube−tube connection, and thus we believe the extent of SEI formation in HCN will be well-prevented and a high Coulombic efficiency is expected. Besides structural integrity

of the HCN, it also possesses a number of other desirable properties as LIB anodes: (1) They are thermodynamically stable and have low kinetic barrier of formation. (2) The channels in HCN are favorable for Li uptake and can reach a high capacity due to the tunable nanoporous size. For example, the estimated Li capacity in (9,0)-HCN can reach 600 mAh/g. (3) The Li-ion diffusion barrier inside the channel is low at ~100 meV. (4) The volumetric expansion upon full lithiation is only ~1%. (5) The atoms at the open ends of the HCN structure would relax to self-close the side walls, leaving nanoporous channels open for Li-ion transport.

## 2. THEORETICAL METHOD

First-principles calculations have been performed to investigate the thermodynamic stability, formation kinetics, and Li storage properties of HCN by using the projector-augmented-wave (PAW)[24] method, as implemented in the Vienna ab initio simulation package (VASP).[25−27] Whereas the local density approximation (LDA) could improve the treatment in the phase diagram of Li intercalated graphite with low concentrations by spuriously mimicking part of the vdW interaction,[28] it is known that LDA severely overestimates the Li−C binding at relatively high concentrations that would affect both the phase stability of Li intercalated compounds and the Li diffusion barriers.[29] We thus choose generalized gradient approximation (GGA) in Perdew−Wang 91 functional for calculating binding energies at different Li concentrations, which is proven to give reliable Li−C interactions in LIB anode materials simulations.[30,31] Additionally, we take into account the dispersion interactions in nanotube bundles, triplets, and HCNs using the Grimme dispersion corrections.[32] This would allow a more accurate prediction of the formation heat and stability comparison between different structures. According to symmetry, the HCNs are modeled using a hexagonal supercell, and the Li atoms are intercalated into these pores along the $c$ axis. The cutoff energy is set to 400 eV, and the Brillouin zones are sampled with a gamma-centered k point mesh of $2 \times 2 \times 12$ for both intrinsic and lithiated HCN. To get the volume change of HCN caused by Li intercalation, all degrees of freedom including cell shape and lattice constants are allowed to relax, and optimal atomic positions are obtained once the magnitude of the Hellmann−Feynman force acting on each atom is <0.05 eV/Å.

## 3. RESULTS AND DISCUSSION

Conceptually, the HCN structure can be thought of as a self-assembly of small diameter SWNTs, where they first rearrange into triplets and then form a hybridized network by joining the reactive tips (Figure 1a). There are two distinct types of carbon atoms within the HCN: the sp³-hybridized carbon atoms (yellow) in the junction regions and sp²-hybridized carbons (gray) as interconnects. The sp³ junctions sit on a hexagonal lattice, very similar to graphene structure from the top-view, except that junctions replace "atoms" and interconnects become "bonds". The enclosed hexagons form 1-D nanoporous diffusion channels along the tube axis ($c$ axis). The pore size of the HCN is tunable by controlling the diameters of SWNTs to be assembled, which makes it appealing in applications such as LIB, hydrogen storage, and quantum sieving.

We begin our discussion from the HCN formation process. One way of forming the HCN structure is via the aggregation of small diameter SWNTs. (5,0) SWNTs, probably at the small
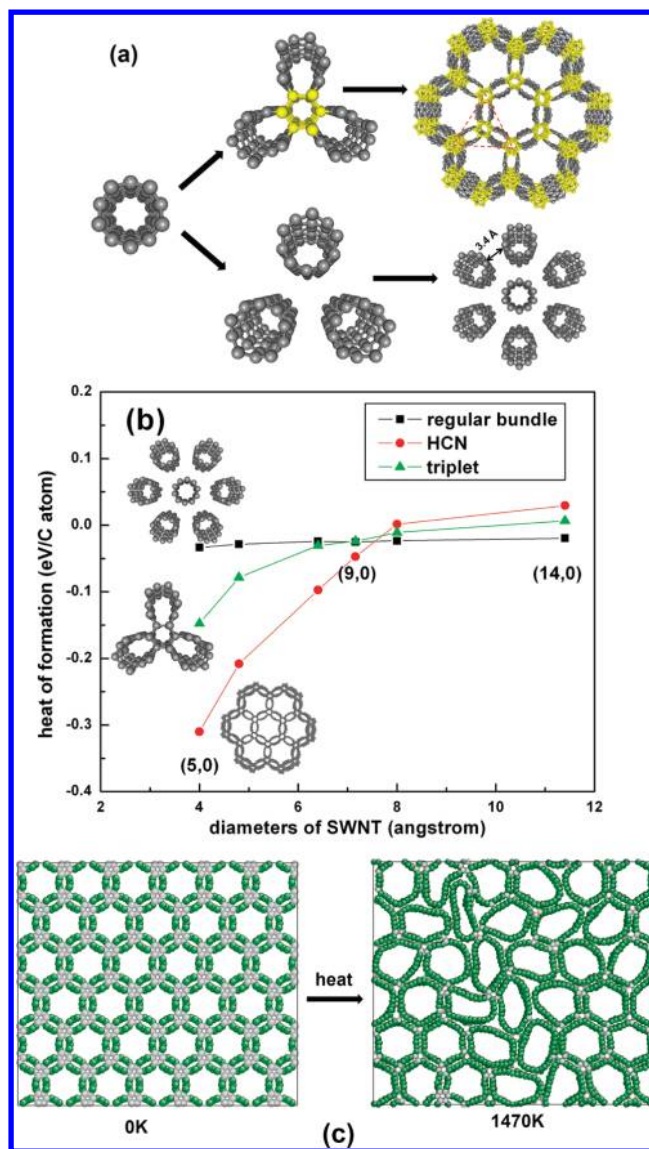


**Figure 1.** (a) Upper model indicates the formations of triplet and HCN by covalent bonding, while the lower model is the formation of a regular bundle by van der Waals force. (b) Calculated heats of formation for HCNs, triplets, and regular bundles as a function of SWNT diameter. (c) Snapshots of (5,0)-HCN at 0 and 1470 K based on molecular dynamics simulations.

diameter theoretical limit, have been fabricated utilizing zeolite templates.[33] In a previous study, we showed that free-standing (5,0) SWNTs prefer to form triplet unity (upper middle model in Figure 1a) connected with chemical bonds rather than weak vdW force due to their intense curvature.[34] However, with increasing number of triplets, the tips of triplets will join each other by chemical bonds and self-assemble into HCN structure. Our total energy calculations indicate that formations of HCN from ultrasmall SWNTs (5,0) are spontaneous, as depicted in the upper path in Figure 1a. The heats of formation for (5,0) triplets and HCN are −0.14 and −0.31 eV per carbon atoms, respectively, where negative values indicate exothermic reactions. Compared with regular bundles of (5,0) SWNT (lower model in Figure 1a), the heat of formation is one order of magnitude larger, primarily due to the formation of 12 covalent bonds per unit cell during this process. The formed (5,0)-HCN has hexagonal symmetry, and the lattice constants $a$

and $c$ are calculated to be 12.8 and 4.2 Å. We find that the formation of such HCN structures is not unique to (5, 0) SWNTs but also applies to other small-diameter zigzag SWNTs (Figure S1 of the Supporting Information (SI)). A comprehensive heat of formation for HCNs and regular bundles as well as single triplet assembled from (5, 0) to (14, 0) SWNTs is shown in Figure 1b. HCNs are substantially lower in energy than regular bundles when the diameter of the constituent SWNTs is smaller than 7.2 Å, that is, a (9, 0) SWNT. Thus, the size of the nanopores in HCN can be tuned by controlling the SWNTs to be assembled and ranges from 1.0 to 1.6 nm. Exceeding the critical SWNT diameter of 7.2 Å, HCN becomes energetically less favorable as compared with regular bundles. As for the kinetic barrier of HCN formation, the sharp curvature of small-diameter SWNTs greatly facilitates its formation. In particular, the ultrasmall diameter (5,0) SWNTs can self-assemble into HCN spontaneously. It also gives us a clue that such HCN structure may also be produced from the well-aligned bundles of SWNTs under the treatment of high pressure. It was previously shown that SWNT can undergo shape transition under pressure, producing anisotropic curvature in the tube wall.[35] A high-pressure (up to 45 GPa) experimental investigation of SWNTs bundles with fullerene encapsulated suggested the SWNTs could transform to multiwall nanocones, nano-onions, and other nanostructure, with extensive strong bonding formation and rearrangement between nanotubes in the process.[36] It is possible that similar chemical bond formation might also happen if high pressure is applied to SWNT bundles. To investigate this possibility, we simulated the shape transition of the (15,0) SWNT bundle upon uniform nonaxial strain and found that the SWNTs would initially undergo hexagonal distortion and eventually phase transform to (5,0)-HCN (Figure S2 of the SI). Molecular dynamics simulations have also been performed using the LAMMPS code[37] with Tersoff potential,[38] and the results indicate that once (5, 0)-HCN is formed it remains stable under ambient temperatures and only transforms back to regular SWNT bundles at an elevated temperature of ~1400 K (Figure 1c and Figure S3 of the SI).

Figure 2a shows the calculated band structure of a (5,0)-HCN. As known, a freestanding (5,0) tube is metallic due to the strong curvature effect.[39] When these SWNTs assemble into a HCN, it becomes semiconducting with a small indirect bandgap of 0.06 eV, where the valence band maximum (VBM) and conduction band minimum (CBM) are located at Γ and K points, respectively. We notice that the band structure of (5,0)-HCN shows obvious anisotropy: the bands in Γ-M-K-Γ directions near the Fermi level are flat across the porous cross-section, suggesting little in-plane dispersion due to the lack of $\pi$-electrons in the junction region that divides sp$^2$ conducting blocks. Along the tube axis, the bands show strong dispersion from Γ to A and are similar to that of a deformed (5, 0) SWNT. These band structure characteristics suggest that the HCN has good electronic conductivity similar to nanotubes. The CBM and VBM states, which are crucial in determining electronics structures, are plotted in Figure 2b,c (upper ones: top-view, bottom ones: side-view). From these Figures, we can further confirm that contribution to both VBM and CBM states primarily comes from sp$^2$ hybrid carbon atoms in the interconnect region, where VBM states show in-plane bonding and antibonding characteristic along the $c$ axis, while CBM shows the opposite.
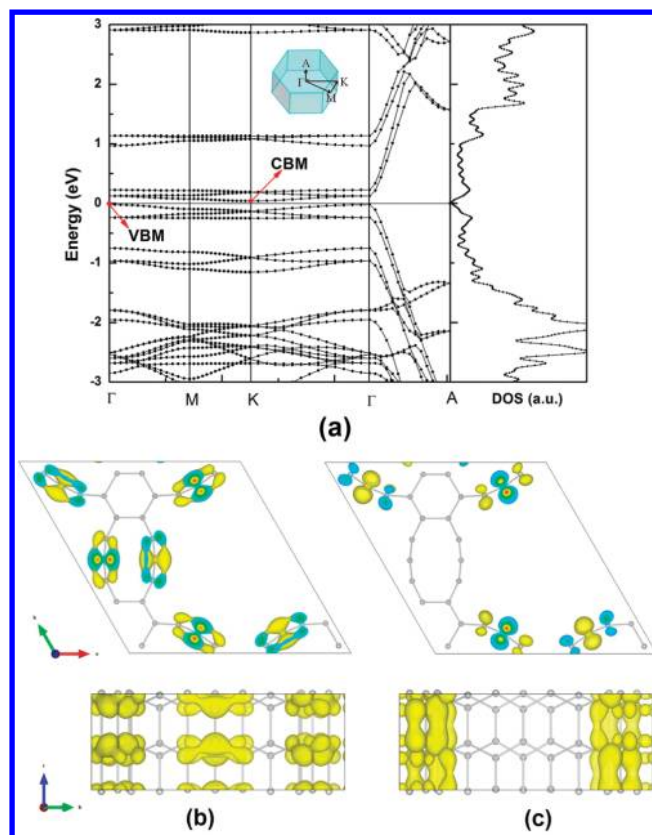


**Figure 2.** (a) Band structure and density of states of a (5,0)-HCN. The inset shows the corresponding path with high symmetric K points in the Brillouin zone. (b,c) VBM and CBM states of the (5, 0)-HCN from both top and side views.

With well-aligned 1-D pores and well-kept electronic conductivity, the HCN may find potential applications in LIB anodes. We thus investigate its Li intercalation properties. We note that there are four high symmetry intercalation sites in HCN, as shown in Figure 3a, conveniently labeled as the corner, side, center, and interior sites. Table 1 summarizes the calculated low-concentration-limit Li binding energies and volumetric changes for the above-mentioned sites, which are defined as:

$$E_b = E_{bundle+Li} - E_{bundle} - E_{Li,bcc}$$

$$\alpha = \frac{V - V_0}{V_0}$$

where $E_{bundle+Li}$, $E_{bundle}$, and $E_{Li\_bcc}$ denote the total energies of Li-intercalated HCN, pristine HCN, and Li in bulk structure (bcc), respectively. $V_0$ and $V$ are the total volume of HCN before and after Li intercalation. From Table 1, it can be seen that the intercalations of Li into the corner and side sites of (5,0)-HCN are the most energetically favorable among the four sites. The center site is ~5 Å away from the sides and thus not favorable for intercalation of a single Li-ion. For the interior site, the space inside the oblate interconnect is too narrow (2.9 Å) to accommodate a Li-ion and induces a strong repulsion between Li and the side walls. The corner and side sites offer suitable distance for Li binding with favorable binding energies. The volumetric changes in all of these cases are negligible. Band structure analysis shows that (5, 0)-HCN becomes metallic
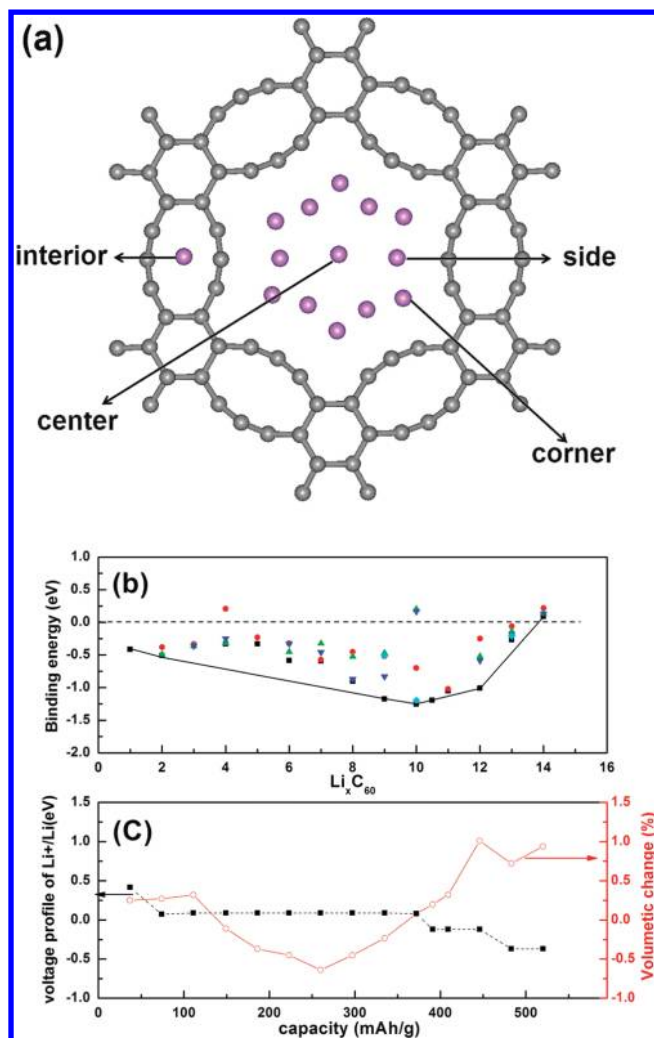
**Figure 3.** (a) Four possible binding sites for Li in a (5, 0)-HCN. (b) Colorful symbols give the calculated Li binding energy of different configurations and constructed black lines of convex hull indicate ground states of (5,0)-HCN with different Li concentrations. (c) Corresponding voltage profile and volumetric change as a function of Li uptake.

**Table 1. Calculated Li Binding Energies and Volumetric Changes for Different Sites in (5, 0)-HCN with Nominal Formula of $LiC_{60}$**

| sites | binding energies (eV/Li) | volumetric changes |
|---|---|---|
| corner | −0.41 | 0.25% |
| side | −0.25 | 0.33% |
| center | 1.01 | 0.31% |
| interior | 0.79 | 0.17% |

upon Li intercalation at relatively low concentrations (Figure S4 in the Supporting Information).

Because of the enhanced structural strength provided by $sp^2$-$sp^3$ bonding hybridizations, it is anticipated that the HCN would undergo only modest volumetric change at high concentration of Li intercalation. First-principles molecular dynamics simulation (computational details can be found in the SI) is utilized to explore the most stable configurations at different Li intercalation concentrations (Figure S5 in the SI), and their binding energies are calculated for Li concentrations ranging from $LiC_{60}$ to $Li_{14}C_{60}$ in Figure 3b. Constructing the

convex hull from the binding energy curve yields the ground states of $Li_xC_{60}$ as a function of Li concentration. The total binding energy initially decreases with increasing Li concentration and eventually saturates. The highest Li intercalation stoichiometry in (5,0)-HCN can reach $Li_{13}C_{60}$ with a favorable negative binding energy, and further Li intercalation will result in positive binding energies. The binding energies of $Li_xC_{60}$ ($x$ from 3 to 8) are above the convex hull, which means those configurations are metastable and will phase separate into $Li_2C_{60}$ and $Li_9C_{60}$. This is responsible for the flat and robust voltage plateau extending to $Li_{10}C_{60}$ (~370 mAh/g) that will be discussed below. We note that the Li capacity is closely related to the size of nanopores, and thus higher capacity can be achieved in HCN with larger nanopores. For example, (9,0)-HCN possesses 1.5 times the pore area of (5,0)-HCN, and thus a capacity of 600 mAh/g can be expected assuming a similar Li volumetric density within the channel.

To evaluate the electrochemical properties of (5, 0)-HCN for LIB anodes, we have calculated the voltage profile by the Faraday laws:

$$Li_xC_{60} + \Delta x Li \rightarrow Li_{x+\Delta x}C_{60}$$
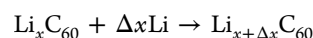
$$V(x) = \frac{-\Delta G}{\Delta x e F}$$

where $\Delta x$ indicates the number of intercalated Li atoms in each step and $F$ is the Faraday constant. The change of Gibbs free energy $\Delta G$ consists of three parts: $\Delta G = \Delta E + P\Delta V - T\Delta S$. In a solid-state reaction, $P\Delta V$ is on the order of $10^{-5}$ eV and $T\Delta S$ is on the order of the thermal energy (~0.026 eV), and thus $\Delta G$ can be well-approximated by using total energies ($\Delta E$) from first-principles calculations.[40] As known, one of the most serious drawbacks of CNT as an LIB anode is the lack of a stable voltage plateau during discharge process.[12,18,41] The robust staged curve of HCN structure can be attributed to the existence of nanopores, which offers stable channels for Li intercalation similar to the interlayer space in graphite. Note that Li-intercalated graphite exhibits three narrower stages in the same range due to the multilayers intercalating mechanism of Li into graphite.[42,43] For HCN, the first plateau has a relatively low $Li^+$/Li potential (0.09 eV) and a wide range (70–370 mAh/g), which implies a high and stable working voltage during discharge process. Another unique property of the HCN structure is its ability to sustain the nanoporous channels without significant expansion/shrinking. Figure 3c (red curve) shows the volumetric change as a function of Li intercalation into (5,0)-HCN. It is worth noting that the volumetric change from $LiC_{60}$ to $Li_{10}C_{60}$ is <1%, about 10 times lower than that of graphite.[44] Our simulations also show that (5,0)-HCN recovers reversibly to the pristine configuration once intercalated Li atoms are removed (Figure S6 in the SI), indicating the good cyclability of HCN during Li insertion/extraction.

Li diffusivity is another important factor affecting the power density and performance of LIB. SWNTs are known to block Li intercalation and diffusion inside the tubes due to their closed ends. In contrast with SWNTs, the open channel of nanoporous HCN can be well-protected and would provide a robust path for Li intercalation and diffusion. Figure 4a shows a relaxed cleaved surface of an open ended (5,0)-HCN. It is found that dangling carbon atoms on the open end self-close the ends of SWNTs (marked as black) due to the curvature effect. As a result, the nanopores of HCN are well-preserved for Li-ion diffusion. The migration barrier of Li atoms moving
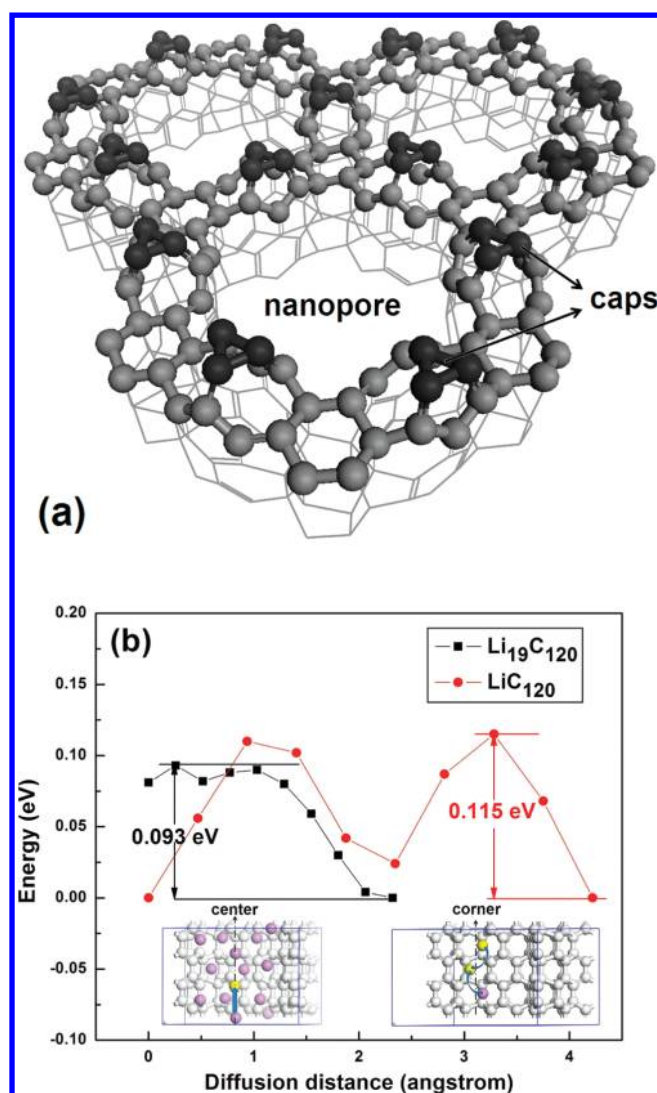
**Figure 4.** (a) Surface reconstruction of cleaved (001) open ends of (5,0)-HCN. (b) Minimum energy path of Li diffusion along nanopores of (5,0)-HCN with formula of $LiC_{120}$ and $Li_{19}C_{120}$. The left inset and right inset indicate the corresponding Li diffusion paths.

along the nanopore is calculated by the nudged elastic band (NEB) method.[45,46] To avoid the interaction of Li-ion with its periodic images, two unit cells are used along the *c* axis. The minimum energy paths of Li moving along the nanopores in $LiC_{120}$ and $Li_{19}C_{120}$ are shown in Figure 4b as representative examples of low and high Li concentration. For $LiC_{120}$, the Li travels from one corner site to another (right inset in Figure 4b) with an energy barrier of 93 meV. For $Li_{19}C_{120}$, The vacancy-mediated Li diffusion barrier is 115 meV when it travels from one center site to another (left inset in Figure 4b). In both cases, the Li migration barrier is much lower than the barrier in graphite (~400 meV),[47] and thus we expect very mobile Li diffusion inside the HCN nanoporous channel that would help improve the LIB power density.

## 4. CONCLUSIONS

We predict a new HCN structure from small SWNTs covalently bonding together based on first-principles calculations. The HCN structure is distinctively different from other graphitic systems held together by vdW interactions and shows

unique hybrid bonding configurations that are favorable for both mechanical robustness and electrical conductivity. Evaluation of its Li storage capacity and electrochemical properties suggests that the HCN structure could be a suitable candidate for next-generation high-capacity, high-power LIB anode.

## ■ ASSOCIATED CONTENT

**Ⓢ Supporting Information**

Description of the detailed computational method and structural information. This material is available free of charge via the Internet at http://pubs.acs.org.

## ■ AUTHOR INFORMATION

**Corresponding Author**

*E-mail: bshan@mail.hust.edu.cn (B.S.); rongchen@mail.hust.edu.cn (R.C.).

**Notes**

The authors declare no competing financial interest.

## ■ ACKNOWLEDGMENTS

## ■ REFERENCES

(1) Nagaura, T.; Tozawa, K. *Prog. Batteries Sol. Cells* **1990**, *9*, 209.
(2) Gao, B.; Bower, C.; Lorentzen, J. D.; Fleming, L.; Kleinhammes, A.; Tang, X. P.; McNeil, L. E.; Wu, Y.; Zhou, O. *Chem. Phys. Lett.* **2000**, *327*, 69−75.
(3) Zhao, J. J.; Buldum, A.; Han, J.; Lu, J. P. *Phys. Rev. Lett.* **2000**, *85*, 1706.
(4) Ishihara, T.; Kawahara, A.; Nishiguchi, H.; Yoshio, M.; Takita, Y. *J. Power Sources* **2001**, *97−98*, 129−132.
(5) Shimoda, H.; Gao, B.; Tang, X. P.; Kleinhammes, A.; Fleming, L.; Wu, Y.; Zhou, O. *Phys. Rev. Lett.* **2001**, *88*, 015502.
(6) Kumar, A.; Reddy, A. L. M.; Mukherjee, A.; Dubey, M.; Zhan, X.; Singh, N.; Ci, L.; Billups, W. E.; Nagurny, J.; Mital, G.; Ajayan, P. M. *ACS Nano* **2011**, *5*, 4345−4349.
(7) Zhou, H.; Zhu, S.; Hibino, M.; Honma, I.; Ichihara, M. *Adv. Mater.* **2003**, *15*, 2107−2111.
(8) Morris, R. S.; Dixon, B. G.; Gennett, T.; Raffaelle, R.; Heben, M. J. *J. Power Sources* **2004**, *138*, 277−280.
(9) Dillon, A. C. *Chem. Rev.* **2010**, *110*, 6856−6872.
(10) Yoo, E.; Kim, J.; Hosono, E.; Zhou, H.; Kudo, T.; Honma, I. *Nano Lett.* **2008**, *8*, 2277−2282.
(11) Cheng, F.; Tao, Z.; Liang, J.; Chen, J. *Chem. Mater.* **2008**, *20*, 667−681.
(12) Chew, S. Y.; Ng, S. H.; Wang, J.; Novák, P.; Krumeich, F.; Chou, S. L.; Chen, J.; Liu, H. K. *Carbon* **2009**, *47*, 2976−2983.
(13) Kaskhedikar, N. A.; Maier, J. *Adv. Mater.* **2009**, *21*, 2664−2680.
(14) Wei, L.; Chen, Q.; Kong, X. *J. Am. Ceram. Soc.* **2011**, *94*, 3078−3083.
(15) Song, B.; Yang, J.; Zhao, J.; Fang, H. *Energy Environ. Sci.* **2011**, *4*, 1379−1384.

4955

dx.doi.org/10.1021/jp3118902 | *J. Phys. Chem. C* **2013**, *117*, 4951−4956

(16) Cambedouzou, J.; Rols, S.; Bendiab, N.; Almairac, R.; Sauvajol, J.-L.; Petit, P.; Mathis, C.; Mirebeau, I.; Johnson, M. *Phys. Rev. B* **2005**, *72*, 041404.

(17) Landi, B. J.; Ganter, M. J.; Schauerman, C. M.; Cress, C. D.; Raffaelle, R. P. *J. Phys. Chem. C* **2008**, *112*, 7509−7515.

(18) Frackowiak, E.; Béguin, F. *Carbon* **2002**, *40*, 1775−1787.

(19) Pan, D.; Wang, S.; Zhao, B.; Wu, M.; Zhang, H.; Wang, Y.; Jiao, Z. *Chem. Mater.* **2009**, *21*, 3136−3142.

(20) Bhardwaj, T.; Antic, A.; Pavan, B.; Barone, V.; Fahlman, B. D. *J. Am. Chem. Soc.* **2010**, *132*, 12556−12558.

(21) Reddy, A. L. M.; Srivastava, A.; Gowda, S. R.; Gullapalli, H.; Dubey, M.; Ajayan, P. M. *ACS Nano* **2010**, *4*, 6337−6342.

(22) Yin, S.; Zhang, Y.; Kong, J.; Zou, C.; Li, C. M.; Lu, X.; Ma, J.; Boey, F. Y. C.; Chen, X. *ACS Nano* **2011**, *5*, 3831−3838.

(23) Yoo, E.; Kim, J.; Hosono, E.; Zhou, H.; Kudo, T.; Honma, I. *Nano Lett.* **2008**, *8*, 2277−2282.

(24) Kresse, G.; Joubert, D. *Phys. Rev. B* **1999**, *59*, 1758.

(25) Kresse, G.; Hafner, J. *Phys. Rev. B* **1993**, *47*, 558.

(26) Kresse, G.; Hafner, J. *Phys. Rev. B* **1994**, *49*, 14251.

(27) Kresse, G.; Hafner, J. *Comput. Mater. Sci.* **1996**, *6*, 15−50.

(28) Rydberg, H.; Jacobson, N.; Hyldgaard, P.; Simak, S. I.; Lundqvist, B. I.; Langreth, D. C. *Surf. Sci.* **2003**, *532*, 606−610.

(29) Kganyago, K. R.; Ngoepe, P. E. *Phys. Rev. B* **2003**, *68*, 205111.

(30) Wen, Y. W.; Liu, H. J.; Tan, X. J.; Pan, L.; Shi, J. *J. Appl. Phys.* **2010**, *107*, 034312.

(31) Liu, H. J.; Li, Z. M.; Liang, Q.; Tang, Z. K.; Chan, C. T. *Appl. Phys. Lett.* **2004**, *84*, 2649.

(32) Grimme, S. *J. Comput. Chem.* **2006**, *27*, 1787−1799.

(33) Wang, N.; Tang, Z. K.; Li, G. D.; Chen, J. S. *Nature* **2000**, *408*, 50−51.

(34) Wen, Y. W.; Liu, H. J.; Pan, L.; Tan, X. J.; Lv, H. Y.; Shi, J.; Tang, X. F. *J. Phys. Chem. C* **2011**, *115*, 9227−9231.

(35) Zang, J.; Treibergs, A.; Han, Y.; Liu, F. *Phys. Rev. Lett.* **2004**, *92*, 105501.

(36) Caillier, Ch.; Machon, D.; San-Miguel, A.; Arenal, R.; Montagnac, G.; Cardon, H.; Kalbac, M.; Zukalova, M.; Kavan, L. *Phys. Rev. B* **2008**, *77*, 125418.

(37) Plimpton, S. *J. Comput. Phys.* **1995**, *117*, 1−19 Code available at: http://lammps.sandia.gov/download.html.

(38) Tersoff, J. *Phys. Rev. B* **1989**, *39*, 5566.

(39) Liu, H. J.; Chan, C. T. *Phys. Rev. B* **2002**, *66*, 115416.

(40) Aydinol, M. K.; Kohan, A. F.; Ceder, G. *J. Power Sources* **1997**, *68*, 664−668.

(41) de las Casas, C.; Li, W. *J. Power Sources* **2012**, *208*, 74−85.

(42) Stevens, D. A.; Dahn, J. R. *J. Electrochem. Soc.* **2001**, *148*, A803−A811.

(43) Persson, K.; Hinuma, Y.; Meng, Y. S.; Van der Ven, A.; Ceder, G. *Phys. Rev. B* **2010**, *82*, 125416.

(44) Whitehead, A. H.; Estrom, K.; Rao, N.; Owen, J. R. *J. Power Sources* **1996**, *63*, 41−45.

(45) Henkelman, G.; Jónsson, H. *J. Chem. Phys.* **2000**, *113*, 9978−9985.

(46) Henkelman, G.; Uberuaga, B. P.; Jónsson, H. *J. Chem. Phys.* **2000**, *113*, 9901−9904.

(47) Persson, K.; Sethuraman, V. A.; Hardwick, L. J.; Hinuma, Y.; Meng, Y. S.; Van der Ven, A.; Srinivasan, V.; Kostecki, R.; Ceder, G. *J. Phys. Chem. Lett.* **2010**, *1*, 1176−1180.